EXPERIMENTAL STUDY OF A DIRECT METHANOL FUEL CELL

M. M. Mench, S. Boslet, S. Thynell, J. Scott, and C.Y. Wang

The Electrochemical Engine Center

Department of Mechanical and Nuclear Engineering

The Pennsylvania State University

University Park, PA 16802

In this investigation, two 50cm^2 direct methanol fuel cells were utilized to obtain detailed performance, flow visualization, and water distribution data. A fractional factorial matrix approach was used to determine the effect of temperature, cathode pressure, stoichiometry, anode flow field configuration, and molarity. Temperature was found to be the dominating factor within the range of conditions tested. Fourier transform infrared (FTIR) spectroscopy was used to examine the water distribution in the cathode as a function of location along the flow path. For low flow rate conditions, cathode flooding was observed. Video microscopy was used to analyze detailed two-phase anode CO_2 bubble behavior, and revealed mechanisms of CO_2 bubble removal from the carbon cloth backing layer. The detailed data and understanding from this investigation should benefit modeling and scale-up efforts in this area.

INTRODUCTION

The liquid-fed direct methanol fuel cell (DMFC) has received enormous interest recently because the DMFC requires less ancillary equipment and is therefore a more simplified system compared to H_2 polymer electrolyte membrane fuel cells (H_2 PEMFC). Several studies have examined the performance of direct methanol fuel cells as a function of operating conditions such as temperature and molarity (e.g., 1-4). Other research has been conducted to observe two-phase flow distribution in the anode of a DMFC (5,6). In addition, several research papers have reported on effluent anode or cathode flow species concentrations using gas chromatography/mass spectroscopy or Fourier transform infrared spectroscopy (7-9). Work performed by one of the authors (Wang) has established an advanced two-phase DMFC model (10). Despite this work, there remains much to be done before the DMFC system is fully understood.

The objectives of this study are to 1) provide detailed experimental data for model validation efforts, 2) develop a diagnostic tool for determination of cathode flooding, and 3) provide baseline data to support system scale-up efforts. In order to accomplish these objectives, two different direct methanol fuel cells, both with 50 cm^2 active area, were utilized.

For detailed species distribution and flow visualization data, a windowed stainless steel cell with a segmented current collecting rib design was used. A schematic of this cell is shown in Figure 1. On both anode and cathode sides, twenty 2 mm wide ribs are embedded in the transparent polycarbonate blocks to form the flow channels. Each rib is welded to a stainless steel rod that is used for current collection from the individual rib location. The flow channels are 2 mm wide, and 2.4 mm deep. A Teflon® gasket was

used to provide sealing. In the anode side transparent polycarbonate, manifolds are located at the top and bottom of the flow field, permitting testing in a parallel or serpentine configuration. Another unique feature of this fuel cell assembly is discrete ports for *ex situ* species extraction via hypodermic needle at nine locations along both the anode and cathode flow paths.

For data to be used to predict performance of a one-kilowatt DMFC scale-up our group is also designing, a titanium DMFC manufactured by Lynntech, Inc. was used. A schematic of this cell is shown in Figure 2. The flow fields for the reactants were a serpentine-parallel combination. On both the anode and cathode inlet, a manifold provided access to six independent (1.5 mm wide and 2.2 mm deep with a rib width of 0.85 mm) serpentine flow channels in parallel with each other.

The membrane electrode assemblies (MEAs) used in this study were manufactured by Lynntech Inc., and had a 4 mg/cm^2 Pt/Ru anode catalyst loading and a 4 mg/cm^2 platinum cathode loading. Nafion 117 was used as the electrolyte.

Schematically shown in Figure 3, the test and control system permits accurate control of anode and cathode cell inlet flow rates, pressure, and relative humidity as well as cell and inlet reactant temperatures. Note that the inlet relative humidity of all cathode flows reported in this study is 0%, and the humidification system was not needed. Cell performance data acquisition was conducted with a twelve-channel Arbin battery/fuel cell testing system. Measurement of anode and cathode species was performed by a Bruker IFS-66/S spectrometer with a 0.96 cm^{-1} resolution. One hundred background scans were averaged with one hundred sample scans to produce transmissivity values for wave numbers between 600 and 3750 cm^{-1}. A 2 µL Hamilton syringe with a 1 % full-scale accuracy was used to take 2 µL samples from the flow field at the sampling ports in the transparent cell. The needle was inserted to the same depth at each port location to ensure each sample was taken from the same depth in the flow field. Samples from the DMFC were injected into a separate sampling chamber for FTIR measurement. The nitrogen-purged chamber is equipped with two uncoated zinc-selenide windows for passage of the infrared beam. FTIR sample chamber temperature was maintained at 120°C for all measurements to ensure vaporization of all species.

RESULTS AND DISCUSSION

A comparison of the performance of the titanium fuel cell and the instrumented transparent fuel cell with stainless steel ribs is shown in Figure 4. It can be seen that the performance of the transparent cell with the stainless steel ribs was lower than that of the titanium cell. The difference in the slopes in the linear region of the polarization curves indicates that the performance loss is mainly attributable to increased contact resistance and ohmic losses associated with the use of stainless steel ribs imbedded in the polycarbonate window. Although performance in the transparent cell is low compared to the titanium cell, high enough current densities can be reached to provide useful data for analysis.

To provide baseline data for system scale-up, data were taken using the titanium cell as a function of several operating parameters. The performance of the titanium cell at a constant flow rate and several pressures is shown in Figure 5. As expected, the voltage output of the cell at a given current density increases with increased pressure, at a constant flow rate. Note, however, that as air pressure is increased and flow rate is kept

constant, the stoichiometry also increases proportionally to the pressure rise. For example, at 0.1 A/cm^2, the 2.7 atm pressure case has a cathode stoichiometry of nearly 55. For the 1.34 atm case, however, the cathode stoichiometry is half of this.

The performance of the titanium cell at operating temperatures ranging from 60^{o}C to 90^{o}C is shown in Figure 6. The performance increases with temperature, as expected, until 80^{o}C. Between 80 and 90^{o}C, however, virtually no additional performance enhancement is seen. This is similar to a result obtained by ref. [2] between 90 and 100 ^{o}C, and is likely a result of increasing methanol crossover at higher temperature. This result indicates that design of a DMFC system for an operating temperature above 80 ^{o}C is not likely to be beneficial, although tremendous performance enhancement can be obtained by increased operating temperature between 60^{o}C and 80 ^{o}C.

Factorial Test Matrix Approach

In order to quantify the effects of cathode pressure, cell temperature, molarity, cathode stoichiometry, anode stoichiometry, and anode flowfield configuration, a fractional factorial (also known as Taguchi) approach was used. These results help to determine the best performance strategy for scale-up with minimal parasitic loss. Details on this method can be found in many experimental design textbooks (e.g. 11). A 2^{6-2} fractional factorial matrix was carried out on the transparent cell so that 16 tests were conducted at every current density tested. Table 1 shows the chosen input parameters and the values chosen for perturbation. Note that all results are applicable only over the range of initial conditions tested, and extrapolation beyond this range is not particularly reliable. In addition, this technique shows the net effect of the perturbation, but will not reveal any peaks or minimums in output that occur between the perturbation values. One test was conducted at each condition. Therefore, the standard error was estimated by averaging the sum of standard errors in each of the 4 and 5 variable higher-order interactions.

Table 2 shows the ratio of the input parameter effect to the standard error. A ratio of >1 indicates that increasing the input parameter has a significant effect in increasing the measured output, *within the range of variable perturbation*. A ratio of < -1 indicates that the input parameter is inversely related to the measured output. Ratios between –1 and +1 indicate the input parameter has little effect on the measured output at the given current density. The chosen measured output is voltage, which was taken for several current density conditions.

Table 1. Input parameter and range of perturbation.

Input parameter	Low value tested	High value tested
Operating temperature	60 ^{o}C	80 ^{o}C
Cathode pressure	1.34 atm	2.7 atm
Anode molarity	0.5	1.5
Anode flow field configuration	Serpentine	Parallel
Anode stoichiometry	5	15
Cathode stoichiometry	10	30

Table 2. Ratio of measured parameter effect to standard error.

i (A/cm^2)	Cath. Press.	Cath. Stoic.	Molarity	Flow field	Temp.	Anode Stoic.
OCV	1.49	-0.42	-7.97	-1.36	3.69	-1.27
0.04	1.89	1.51	-0.70	0.05	5.73	0.58
0.08	1.29	1.40	2.98	-0.01	7.18	1.43
0.1	-0.34	1.05	2.91	-0.33	5.18	0.30

At all conditions tested except open circuit, temperature was the dominant variable affecting output voltage at a given current density. Increasing cathode pressure is positively related to voltage at open circuit conditions, and its effect on output decreases as current density is increased, even showing a non-significant relationship at 0.1 A/cm^2. This interesting result can be explained by considering that *at a given stoichiometry*, as pressure is increased, flow rate is necessarily decreased. Since the rate the cathode flow can remove water vapor from the backing layer is directly proportional to the flow rate, increased pressure results in a decreased ability to remove water, and increased likelihood of cathode flooding. Since water creation/arrival at the cathode in the DMFC is dominated by electro-osmotic drag and reduction reaction as current density increases, it is expected that flooding will be worse at higher current density. This trend is indeed shown by the results listed in Table 2.

Molarity was determined to be inversely related to voltage at open circuit conditions, and have a positive relationship at higher current densities, when more methanol is consumed by reaction. Interestingly, anode flowfield configuration (parallel and serpentine configurations were tested), and anode stoichiometry have minimal effect on performance. The anode stoichiometry was well above that needed (5 or 15), explaining this result. In view of the insensitivity of anode flowfield configuration on performance up to 0.1 A/cm^2, it is clear that anode-side mass transport limitations and CO_2 blockage of reactant sites did not occur. As expected, open circuit voltage is most strongly affected by molarity and temperature.

Bubble Behavior Observations

Anode behavior was observed using a Pulnix TM-9701 CCD camera and a Volpi AS 13/50 microprobe. Cathode behavior was observed using the Pulnix camera and a Canon 12.5-75 mm lens. Low current densities of 0.04 A/cm^2 and 0.10 A/cm^2 were used to visualize the bubbles, due to their high frequency of generation and release at higher current densities.

On the anode side, gas bubble growth and ejection from the backing layer/flow channel interface region was observed to occur in two general locations with correspondingly different behavior: 1) between the current collecting ribs in the middle of the flow channel or 2) attached to them. Midway between current collection ribs, various discrete locations of high activity were found, where the carbon cloth weave had relatively large openings. Bubbles on the order of 0.1 to 0.5 mm were observed to evolve from several different locations within the backing layer. These bubbles had a tendency to remain separate, and detached from the carbon cloth to enter the flow channel by forced-liquid flow. An increase in the current density from 0.04 to 0.1 A/cm^2 immediately increased the frequency of bubble creation, but did not alter bubble size.

Bubble growth near the stainless steel rib-backing layer interface resulted in much larger slugs that absorbed surrounding bubbles before departure from the backing layer

into the free stream. Small gas bubbles, evolved from beneath or near the larger slug, coalesce with the slug, resulting in a pulsed growth behavior observed on video of the event. Rather than a smooth expansion, these slugs were observed to grow in discrete pulses, at regular intervals. At lower current densities, these rib slugs grew to sizes of 1-5 mm and tended not to break free from the rib location until absorbed by a larger slug of coalesced gas from the freestream. When the current density was increased, at the same flowrate, the rib slugs grew faster, but did not grow as large because they had a greater tendency to break free from the corner without the assistance of a large slug. This is likely due to momentum effects from the rapidly arriving CO_2 bubbles. Pictures of various sizes of anode-side CO_2 bubbles are shown in Figure 7. In summary, CO_2 bubble removal from the anode backing layer occurs by two mechanisms: 1) flow-induced removal and 2) large gas bubble coalescence.

On the cathode side, it is difficult to visualize the MEA surface due to fogging of the window. Therefore, a lower magnification lens was used to observe the entire flowfield. Small, 0.5-1 mm sized liquid water droplets were observed on the inner surface of the transparent windows. These apparently were the result of dripping and not condensation, as they were observed to appear suddenly at irregular intervals. Droplets tended to occur over the latter half of the serpentine cathode path, as a result of greater water saturation.

Determination of Cathode Flooding

Additional study was performed to develop a diagnostic tool for determining the presence and location of cathode flooding. Figure 8 is a polarization curve for the transparent cell with two different flow rates. The two flow rates correspond to cathode stoichiometries of 2.14 and 4.29 at 0.12 A/cm^2. While some of the drop in performance for the low flow rate case is probably a result of concentration polarization, flooding also occurred. FTIR measurements were taken for both flow rate cases at several different locations within the cathode flow path at 0.12 A/cm^2. Each measurement was repeated three times, to ensure accuracy. Figure 9 is a plot of the measured transmissivity, at three separate wave numbers, versus distance along the flow path for the higher flow rate case, shown in Figure 8. The transmissivity at all three wave numbers monotonically decreases with distance along the flow path, indicating an increasing water vapor content. It should be noted that the transmissivity is not linearly related to the mole fraction and thus the mole fraction distribution is similar, but not identical to Figure 9. Figure 10 is a plot of the measured transmissivity versus distance along the flow path for the lower flow rate case shown in Figure 8. The transmissivity values reach a plateau at all three wave numbers at distance greater than about half of the 1380 mm cathode serpentine path length, indicating that no additional moisture accumulation is taking place. This indicates that the cathode flow has reached saturated conditions, and cathode flooding is occurring.

In order to provide additional evidence that the poor performance was a result of cathode flooding and not concentration polarization, tests were conducted to measure transparent cell output at identical stoichiometries and different flow rates, as shown in Figure 11. Cathode stoichiometry was kept constant for two different flow rates by varying pressure. Despite identical stoichiometry and higher cathode-side pressure, which should increase performance through increased reactant activity and decreased methanol crossover, performance for the lower flow rate case is much worse and shows the same general trend as the flooded case of Figure 8. In this case, the reduced flow rate at higher pressure resulted in decreased performance from cathode flooding, more than eliminating and gains from increased activity or decreased crossover.

Compared to the lower performing transparent cell, it is observed that the titanium cell had a higher flow rate threshold for avoiding cathode flooding performance losses. A polarization curve taken for the titanium cell at various cathode flow rates is shown in Figure 12. The higher threshold flowrate for avoiding flooding losses is expected, because electro-osmotic drag and reduction reaction dominate water arrival/production at the cathode surface. Thus, it is expected that the water removal required to avoid flooding from the cathode backing layer increases with current density.

CONCLUSIONS

The performance of a titanium 50 cm^2 DMFC increased with temperature from 60 to 80 ^oC, with no additional increase in performance at 90^oC. A fractional factorial matrix approach was used to determine that, within the range of initial conditions tested, anode flow rate and flowfield configuration had little effect on performance, while temperature was the most dominating parameter affecting performance. CO_2 bubbles, on the order of 0.1 to 0.5 mm, were observed evolving from the carbon cloth backing layer, while much larger static slugs were observed to grow in a pulsing fashion attached to rib locations. Bubble removal from the backing layer occurred by two phenomena: 1) liquid flow-induced removal and 2) coalescence of bubbles. A new diagnostic tool for identification of flooding with *ex situ* FTIR measurements was introduced. Flooding was observed at low flow rate, high current density conditions.

ACKNOWLEDGEMENTS

The authors wish to gratefully acknowledge funding for this research from the Pennsylvania Department of Environmental Protection, The United States Department of Transportation Advanced Vehicle Program, and The Mid-Atlantic Regional Consortium for Advanced Vehicles (MARCAV).

REFERENCES

1. K. Scott, W. M. Taama, and J. Cruickshank, *J. Applied Electrochemistry*, **28**, 289 (1998).
2. M. Baldauf and W. Preidel, *J. Power Sources*, **84**, 161, (1999).
3. H. Dohle, J. Diisek, and R. Jung, *J. Power Sources*, **86**, 469, (2000).
4. X. Ren, T. E. Springer, and S. Gottesfeld, *J. Electrochem. Soc*., **147**, (1), 92, (2000).
5. P. Argyropoulos, K. Scott, and W. M. Taama, *Electrochimica Acta*, **44**, 3575 (1999).
6. P. Argyropoulos, K. Scott, and W. M. Taama, *J. Applied Electrochemistry*, **29**, 661 (1999).
7. J.-T. Wang, S. Wasmus, and R. F. Savinell, *J. Electrochem. Soc*., **143**, (4), 1233, (1996).
8. W.-F. Lin, J.-T. Wang, and R. F. Savinell, *J. Electrochem. Soc*., **144**, (6), 1917, (1997).
9. Q. Fan, C. Pu, K. L. Ley, and E. S. Smotkin, *J. Electrochem. Soc. Letters*, **143** (2), L21, (1996).
10. Z. H. Wang and C. Y. Wang, *Proceedings of the 199th ECS*, (2001).
11. P. J. Ross, *Taguchi Techniques for Quality Engineering*, McGraw Hill, New York (1996).

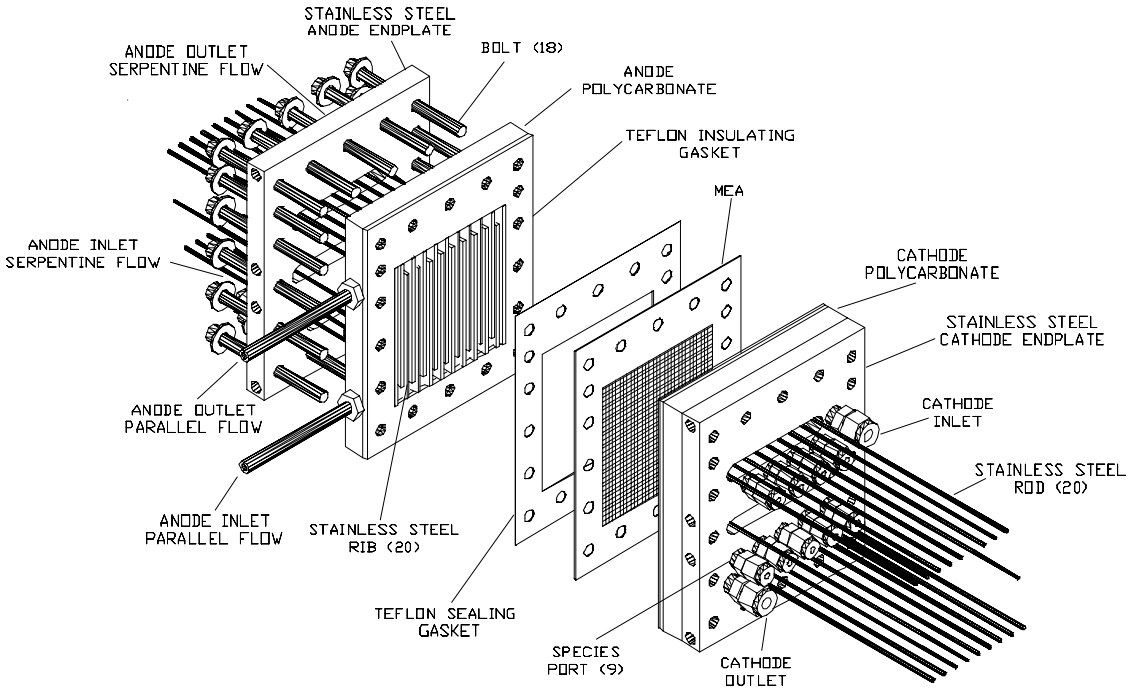

Figure 1. Schematic of the transparent, instrumented stainless steel 50 cm^2 DMFC used for detailed diagnostics and flow visualization.

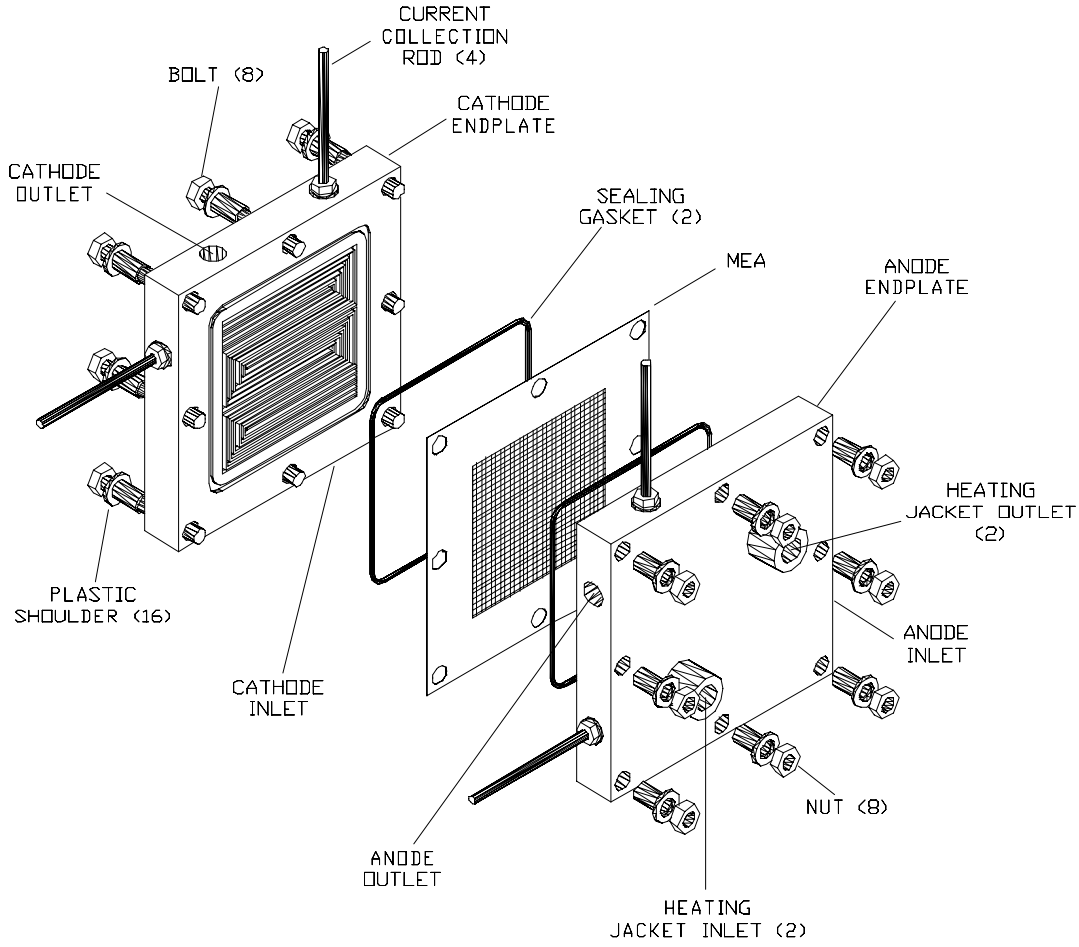

Figure 2. Schematic of the titanium 50 cm^2 DMFC used for performance characterization.

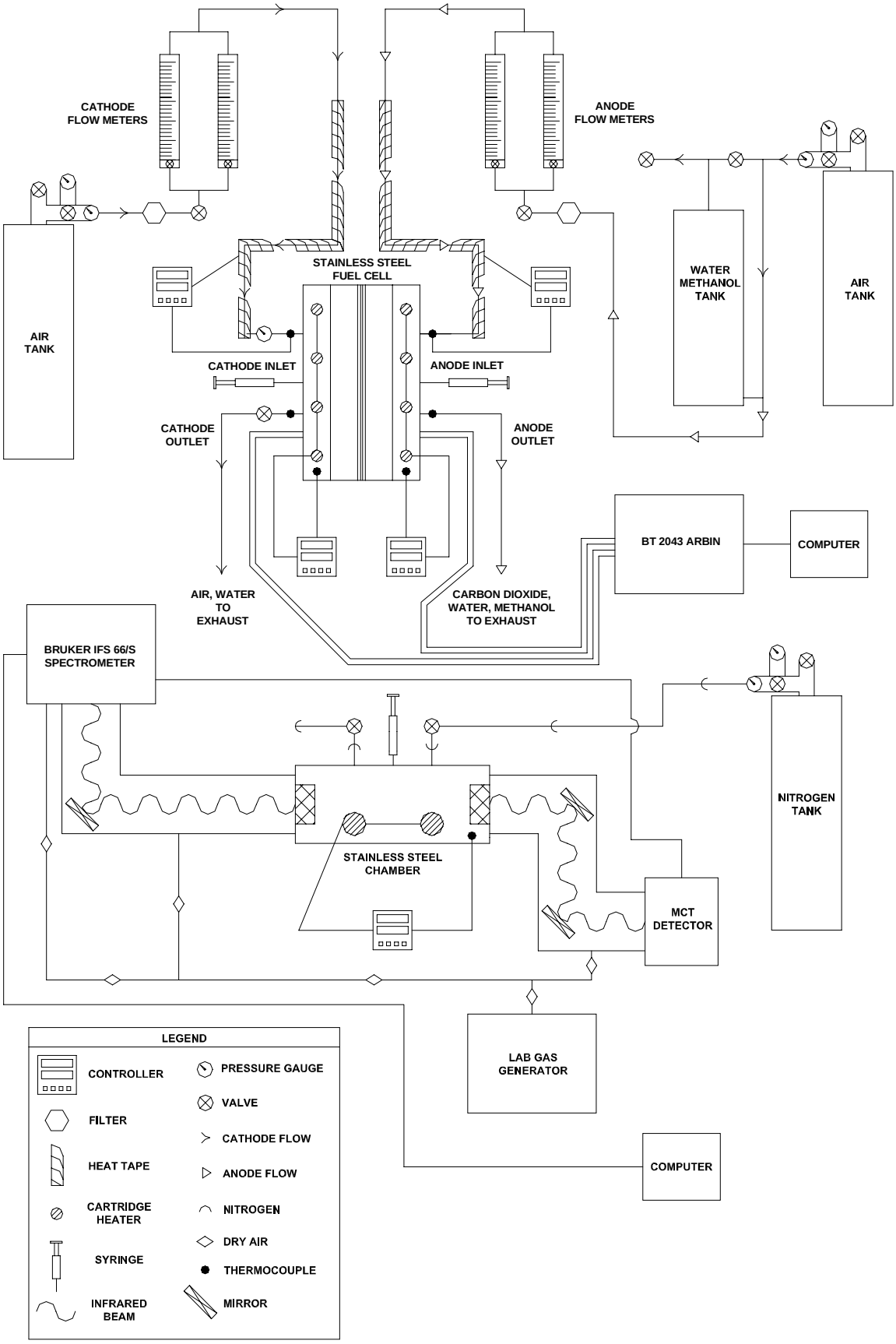

Figure 3. Schematic of control system of stainless steel DMFC and FTIR setups.

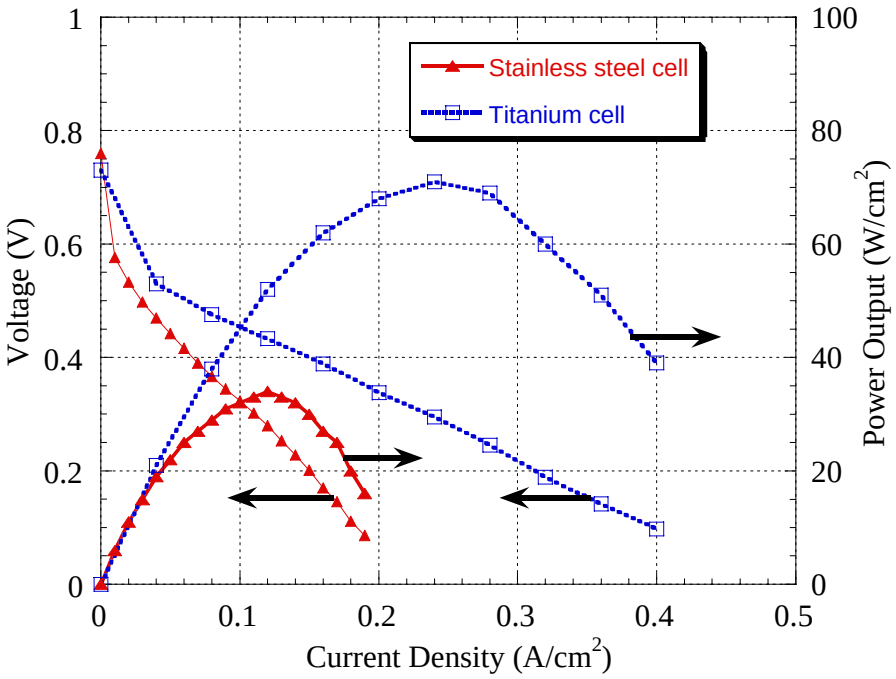

Figure 4. Performance comparison of transparent stainless steel cell and titanium cell. Operating conditions: 1.0 M solution, temperature: 70^{o}C, anode methanol solution stoichiometry: 10, air cathode stoichiometry: 50, anode exit pressure: 1 atm, cathode exit pressure: 2.02 atm.

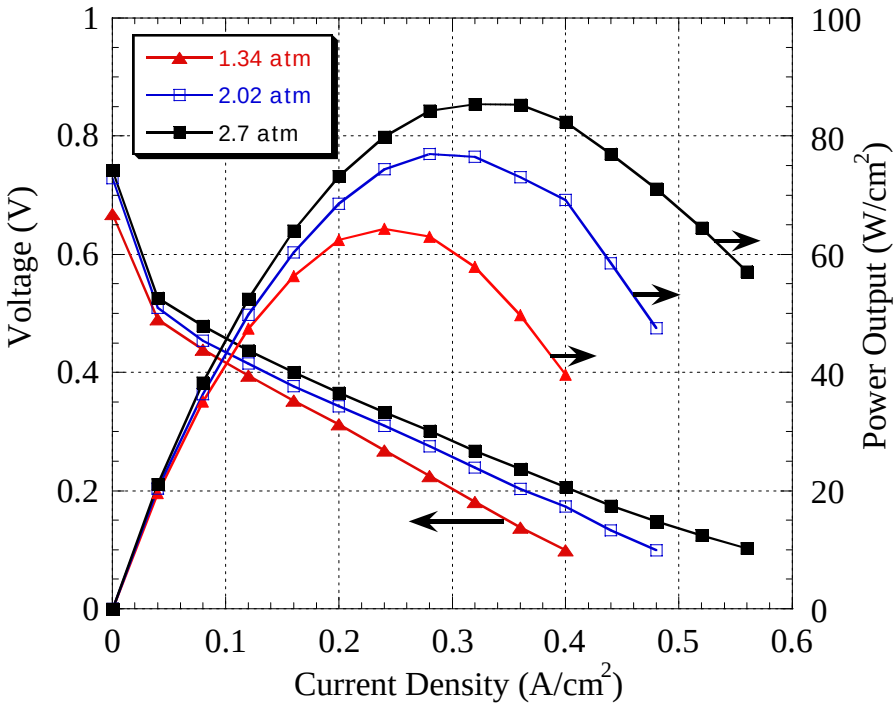

Figure 5. Performance of titanium DMFC as a function of cathode operating pressure. Operating conditions: 1.0 M solution, temperature: 70^{o}C, anode flowrate: 14 mL/min, cathode air flowrate: 2100 mL/min, anode exit pressure: 1 atm.

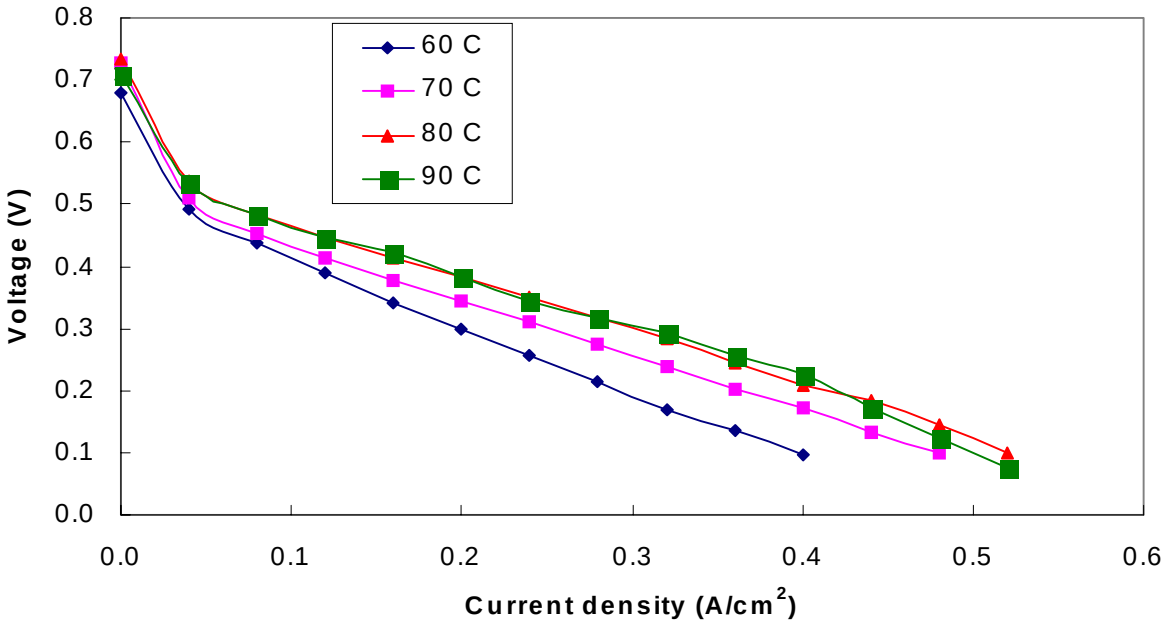

Figure 6. Performance of titanium DMFC as a function of cathode operating temperature. Operating conditions: 1.0 M solution, anode flowrate: 14 mL/min, cathode air flowrate: 2100 mL/min, anode exit pressure: 1 atm, cathode exit pressure: 2.02 atm.

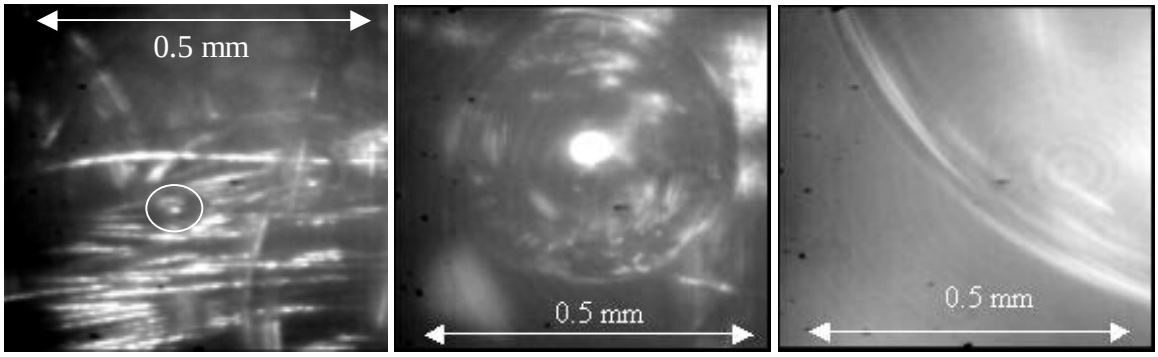

(a) (b) (c)

Figure 7. Pictures of anode-side CO_2 bubble (a) emergence from the backing layer with small-size (b) emergence from the backing layer with large-size and (c) large sized accumulation attached to a current collecting rib.

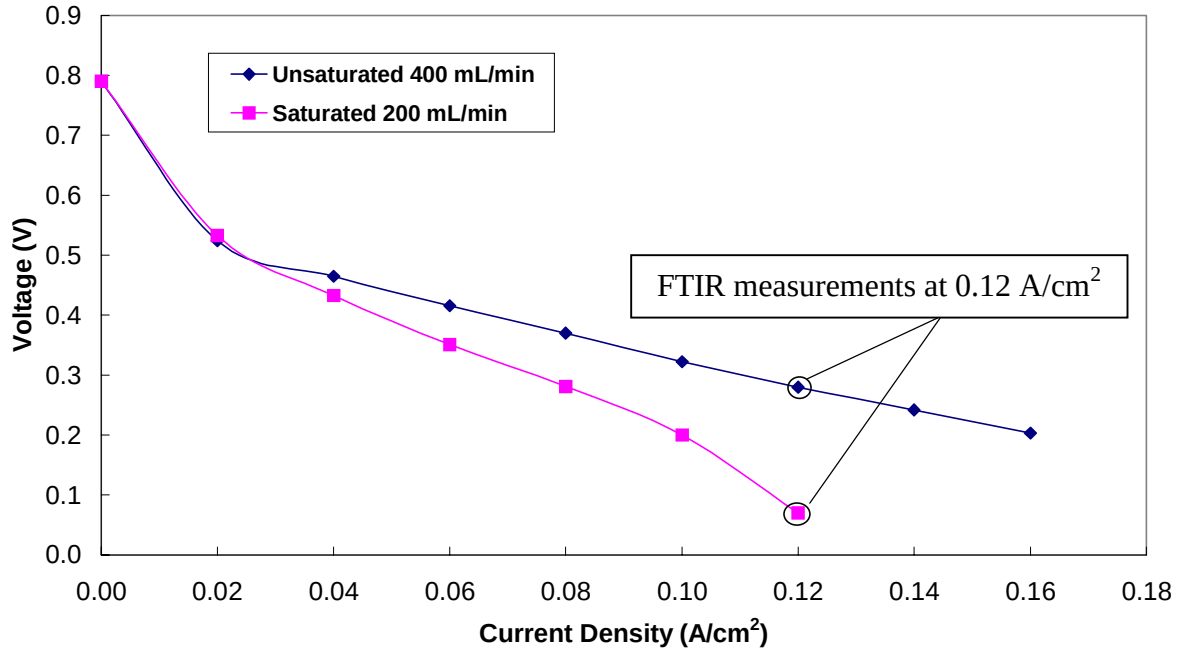

Figure 8. Polarization curve for two different cathode flow rates in the transparent cell, showing effects of flooding. Operating conditions: 1.0 M solution, temperature: 70°C, anode flowrate: 14 mL/min, cathode air flowrate: 200, 400 mL/min, anode exit pressure: 1 atm, cathode exit pressure: 1.34 atm.

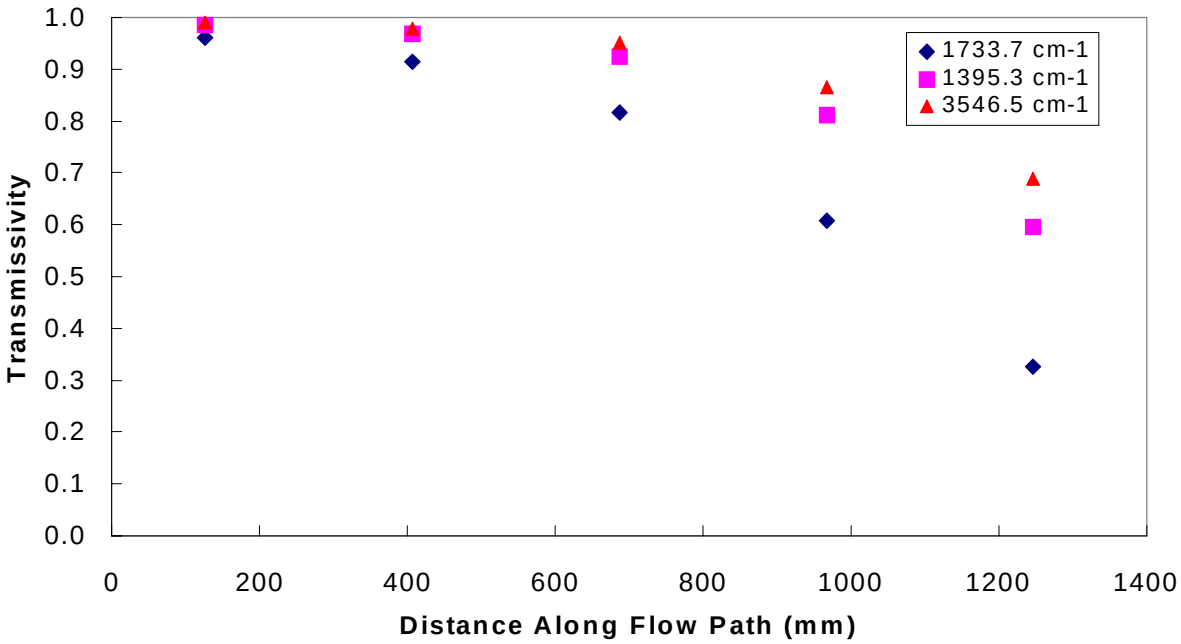

Figure 9. Measured transmissivity versus distance along the cathode flow path for high (400 mL/min) flow rate case shown in Figure 8, showing steady accumulation of water vapor along the flow path from inlet to exit at 1380 mm.

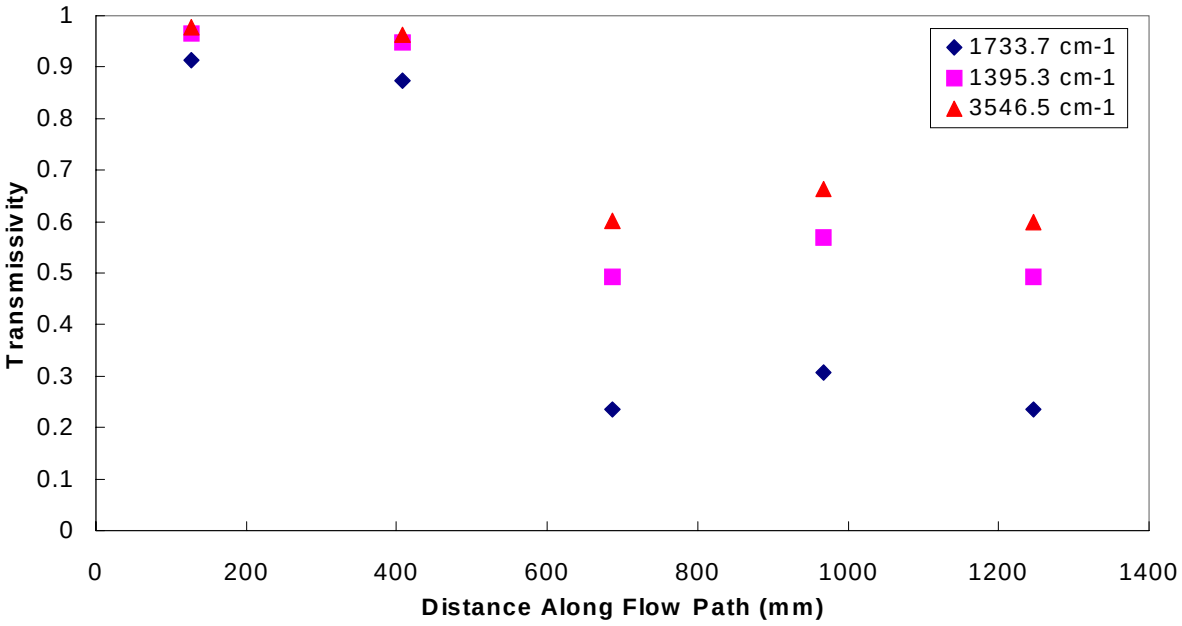

Figure 10. Measured transmissivity versus distance along the cathode flow path for low (200 mL/min) flow rate case shown in Figure 8, showing an eventual plateau indicative of saturated humidity conditions.

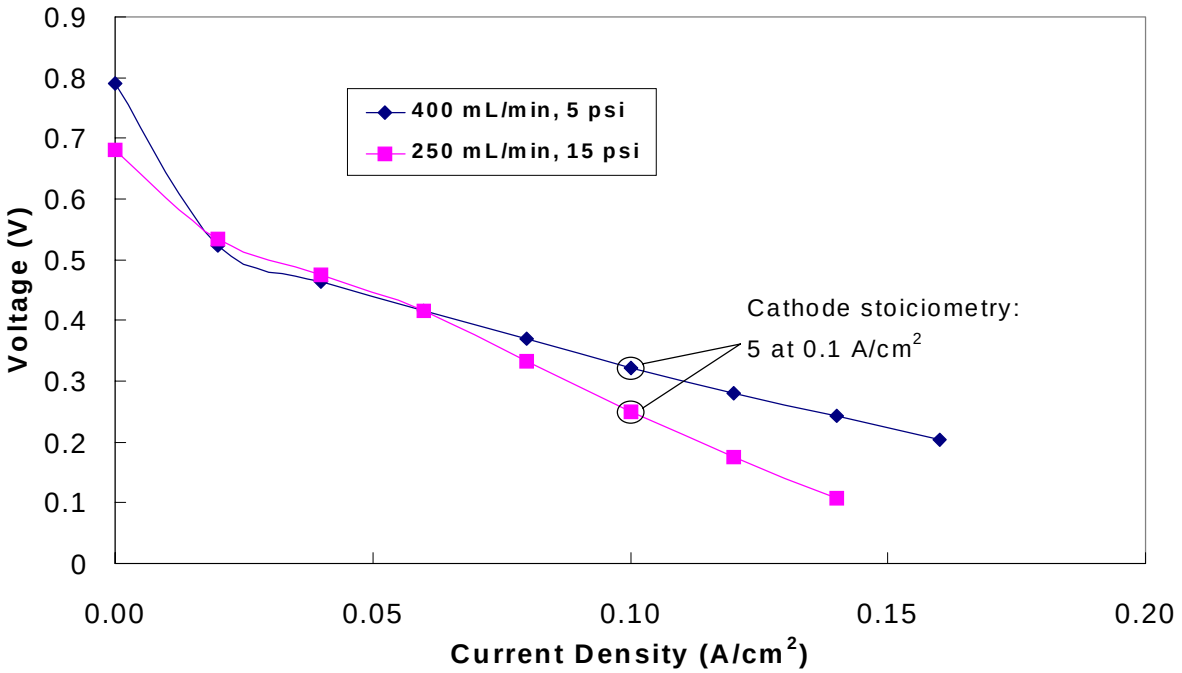

Figure 11. Polarization curve for two different cathode pressures and identical stoichiometries in the transparent cell, showing effects of flooding. Operating conditions: 1.0 M solution, temperature: 70°C, anode flowrate: 14 mL/min, cathode air flowrate: 250, 400 mL/min, anode exit pressure: 1 atm, cathode exit pressure: 1.34 and 2.02 atm.

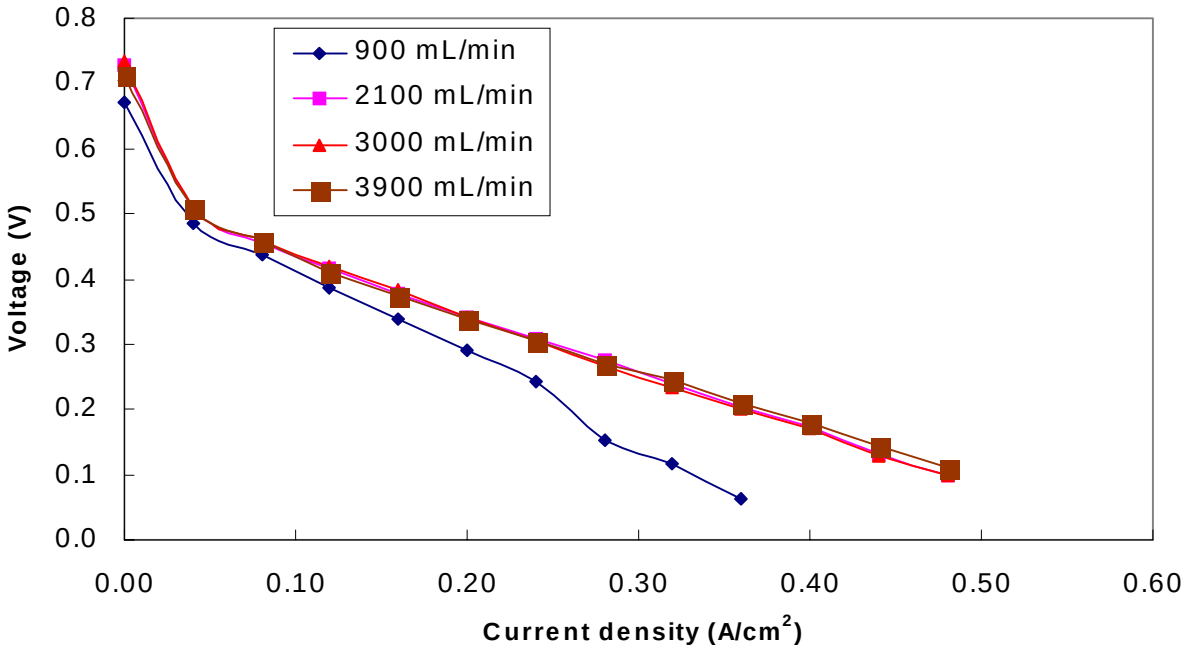

Figure 12. Polarization curve for several different cathode flowrates in the titanium cell, showing effects of flooding at high current density. Operating conditions: 1.0 M solution, temperature: 70°C, anode flowrate: 14 mL/min, anode exit pressure: 1 atm, cathode exit pressure: 2.02 atm.